Article

Burrow Opening Measurements of Intertidal Macroinvertebrates from Optical Drone Images

Su-Bin Ha [1], Yeongjae Jang [2] (ID), Jaehwan Seo [3] (ID), Keunyong Kim [2], Bon Joo Koo [3] (ID), Joo-Hyung Ryu [2] and Seung-Kuk Lee [1,*]

[1] Division of Earth Environmental System Sciences, Pukyong National University, Busan 48513, Republic of Korea; subin@pukyong.ac.kr
[2] Korea Ocean Satellite Center, Korea Institute of Ocean Science & Technology (KIOST), Busan 49111, Republic of Korea; yeongjae@kiost.ac.kr (Y.J.); keunyong@kiost.ac.kr (K.K.); jhryu@kiost.ac.kr (J.-H.R.)
[3] East Sea Environment Research Center, Korea Institute of Ocean Science & Technology (KIOST), Uljin 36315, Republic of Korea; playersjh@kiost.ac.kr (J.S.); bjkoo@kiost.ac.kr (B.J.K.)
* Correspondence: seungkuk.lee@pknu.ac.kr

Abstract: Intertidal macroinvertebrates, such as crabs and mud shrimps, are invertebrates inhabiting the intertidal zone that are sufficiently large to be identified with the naked eye. Most intertidal macroinvertebrates typically construct burrows of various shapes in sediment to protect themselves from environmental extremes, with surface openings that reflect features of their species and body size. Especially circular burrow openings correlate with an organism's body size; thus, measuring these openings can provide estimates of the organism's size, weight, growth rate, and biomass. Traditional studies of these organisms have relied on field surveys, which are constrained by time, cost, and logistical limitations. This study introduces an innovative method for measuring the burrow opening diameters of intertidal macroinvertebrates using high-resolution optical images from a portable drone system. By leveraging the reflectance disparity between the sediment and burrow openings, this method facilitates the extraction and sizing of burrow openings. Our methodology was applied to three crab species known for their circular burrow opening: the red-clawed fiddler, the milky fiddler, and the ghost crab. Validation was confirmed through field data from the Mageumri and Sinduri tidal flats, South Korea. The method achieved a correlation coefficient (R^2) of 0.94 and a root mean squared error (RMSE) of 1.68 mm across a diameter range of 6.21–33.59 mm. These findings suggest the potential of drone remote sensing systems as a non-invasive and efficacious approach for quantifying burrow sizes over extensive intertidal areas, thereby facilitating more accurate biomass estimations and surmounting the limitations of conventional field surveys. Future research could extend this method to additional species and further refine its precision.

Keywords: burrow opening; intertidal macroinvertebrate; drone; tidal flat

1. Introduction

Tidal flats, dynamic coastal regions alternating between submersion and exposure, play a pivotal role in various ecological processes and are integral to both cultural heritage and environmental conservation. These areas are not only significant blue carbon sinks, sequestering atmospheric CO_2 and storing organic carbon [1–3], but they are also characterized by a dynamic flow of organic matter, fueled by the high productivity of benthic algae and phytoplankton [4,5]. The utilization of this organic matter by the resident benthic organisms [6] significantly influences the carbon dynamics within these flats.

The interactions among tidal flat organisms, including the decomposition processes and the physicochemical and biological conditioning of the sediment, are critical to the functioning of these ecosystems [7]. Macrobenthic organisms, a major biological component of tidal flat ecosystems, profoundly affect these processes [8]. As bioturbators, they engage in burrowing, feeding, respiration, and excretion, which not only impact sediment

properties but also regulate the flow of organic matter [9–15]. Intertidal macroinvertebrates are particularly instrumental in this dynamic. Their activities, especially burrowing, play an essential role in modulating the carbon dynamics by altering sediment structure and influencing microbial activities. These burrows help manage the processing of organic carbon in tidal flats [16–19].

Traditionally, studies on intertidal macroinvertebrates have relied on field surveys to count and measure burrow openings [20], using these data to extrapolate biomass across tidal flats [21,22]. However, despite recent advances demonstrating a correlation between burrow opening dimensions and biomass [23,24], the comprehensive, in situ estimation of organism abundance over vast tidal flats remains a challenge.

Remote sensing techniques have offered a non-invasive alternative for studying extensive areas [25,26], with high-resolution data providing insights into ecosystem dynamics [27]. Historical reconstruction of tidal flat topography [28] and global substrate analysis over decades [29] have been achieved using optical satellite imagery. However, the spatial resolution limitations of civilian satellites, such as Pleiades or Ikonos, are compounded by cost, cloud cover, and acquisition constraints [30]. The resolution provided by optical satellite imagery, which ranges from tens of centimeters to meters, is often inadequate for detailed measurements of small features, such as burrow openings. To address these challenges effectively, drones equipped with high-resolution sensors have proven to be indispensable [31,32]. These advanced unmanned aerial vehicles (UAVs) provide a critical bridge over existing observational gaps, enabling highly precise measurements of small-scale features, such as burrow openings [33–36]. This technology facilitates detailed and accurate data collection that is essential for understanding the intricate dynamics of these features.

By integrating advanced remote sensing techniques with high spatial resolution and analytical methods, including artificial intelligence, it is now possible to achieve a more detailed and nuanced understanding of tidal flat dynamics [37–39]. Recent advancements in drone imaging technology have enabled the acquisition of high-resolution optical images with resolutions down to a few millimeters. Utilizing drone imagery of the tidal flat surface combined with machine learning has enhanced species classification and detailed analysis of tidal flat dynamics, including for three crab species: the red-clawed fiddler crab, the milky fiddler crab, and the ghost crab [40,41].

The burrow opening size and species composition of burrow inhabitants facilitate the analysis of tidal flat biodiversity, spatial distribution, and seasonal variations [42]. This is a non-intrusive technique for estimating the abundance and analyzing the growth rate of intertidal macroinvertebrates across a large area, utilizing portable drone systems. Moreover, these quantitative analyses enable the monitoring of a broad spectrum of life forms. This spectrum encompasses not only the residents of tidal flats but also the apex predators, such as migratory birds, that rely on these habitats for survival. This monitoring is essential for developing strategies to preserve their ecological integrity and ensure their continued contribution to environmental sustainability and biodiversity.

Our study contributes to this growing body of work by presenting a novel methodology that utilizes high-resolution drone optical imagery to measure circular burrow openings. We developed a technique that leverages the red, green, and blue spectral bands to accurately gauge the size of burrow openings, with validation against in situ measurements.

2. Study Area and Data

2.1. Study Area

This study was conducted on the west coast of Korea, focusing on two key locations: the Mageumri and Sinduri tidal flats (Figure 1). These sites were selected for their abundant macroinvertebrate populations and the habitats they offer to the species under investigation. The Mageumri tidal flats are distinguished by fine sandy substrates that support the red-clawed fiddler crab (*Uca arcuata*) and milky fiddler crab (*Uca lactea*), while the Sinduri tidal

flats, adjacent to extensive coastal dunes, feature predominantly sandy zones favorable to the ghost crab (*Ocypode stimpsoni*).
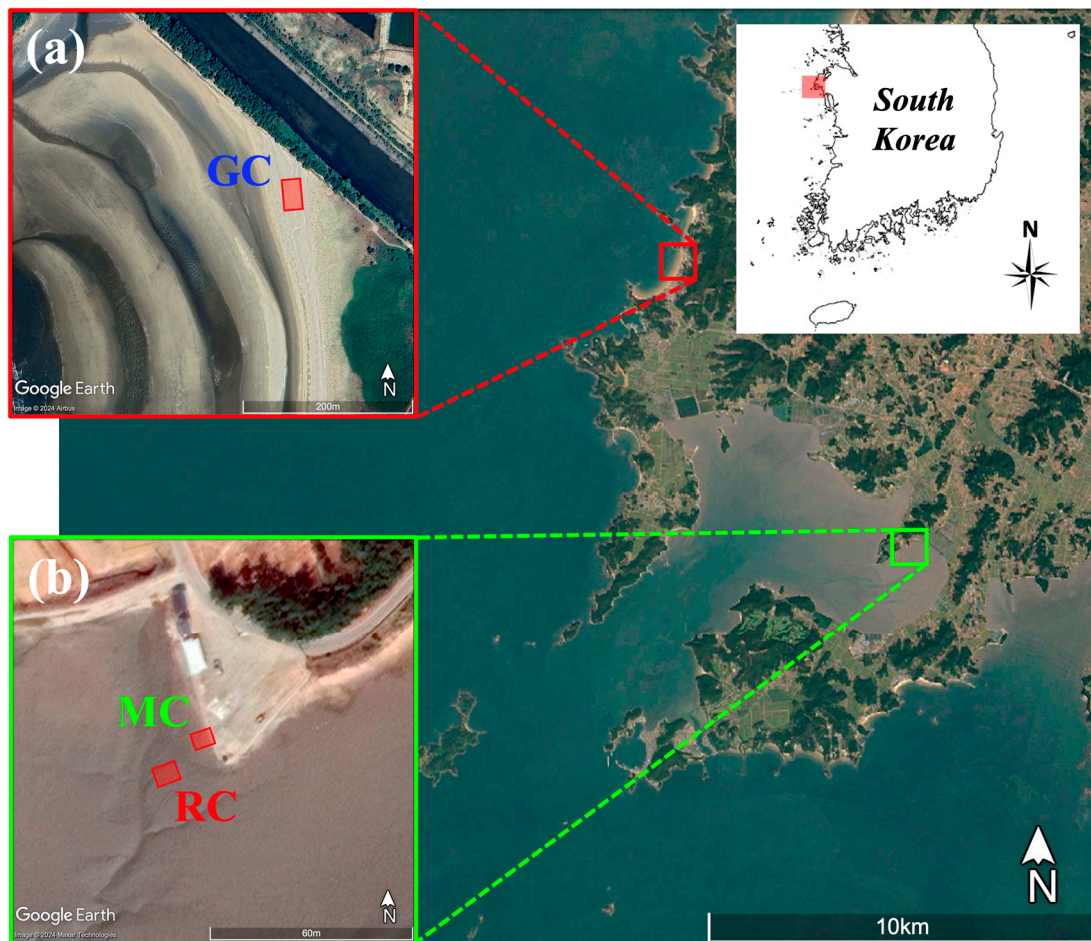

Figure 1. Locations of two study areas along the west coast of Korea. (**a**) Sinduri tidal flat (GC: ghost crab), (**b**) Mageumri tidal flat (RC: red-clawed fiddler crab, MC: milky fiddler crab). Data source: Google Earth.

In August 2022, field surveys were conducted to study these three species (Figure 2). Drone imagery was captured at the Mageumri tidal flats, noted for their muddy composition, where fiddler crabs are observed during low tide, engaging in surface activities typical of tropical and subtropical flats [43,44]. The burrows of these crabs, transversely consistent in their circular shape, are a distinctive feature of the landscape [45]. At the Sinduri tidal flats, with their sandy texture [46], we collected imagery of ghost crab burrows [47]. Ghost crabs, primarily nocturnal foragers, retreat to their circular burrows during the day. The morphology of these burrows, often surrounded by sand mounds and radial feeding lines, reflects the crabs' burrowing and foraging behaviors [48]. The presence and structure of these burrows are integral to the tidal flats' ecosystem, contributing to sediment aeration and nutrient cycling.
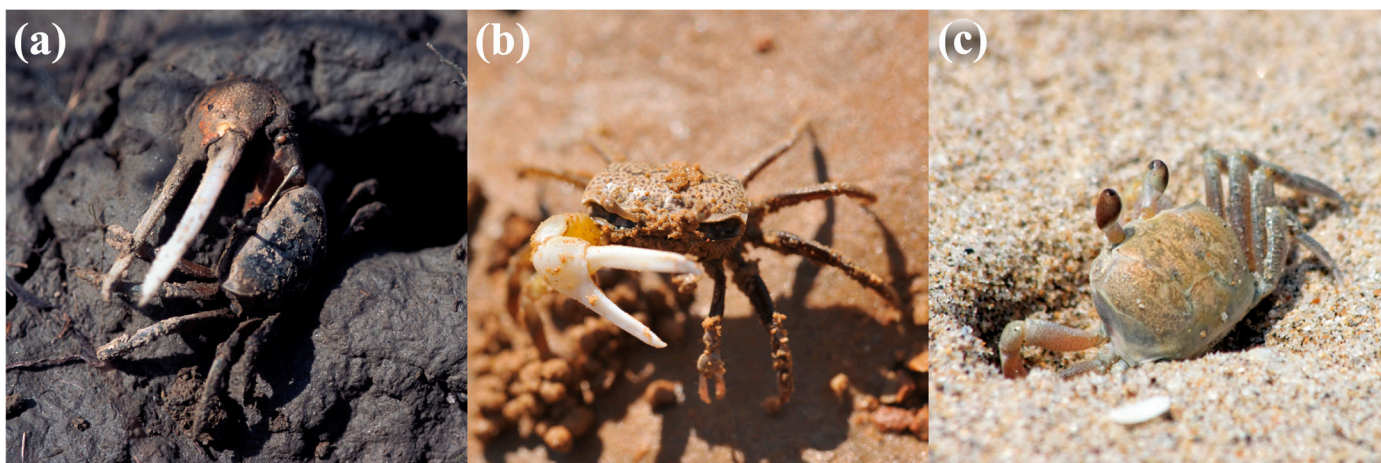
Figure 2. The researched species: (**a**) red-clawed fiddler crab (*Uca arcuata*), (**b**) milky fiddler crab (*Uca lactea*), and (**c**) ghost crab (*Ocypode stimpsoni*).

2.2. Dataset

2.2.1. Drone Image

For this research, high-resolution visible light imagery was acquired using a Matrice 300 RTK drone (DJI, Shenzhen, China), outfitted with a Zenmuse P1 RGB sensor (35 mm fixed-focus lens; (DJI, Shenzhen, China). To achieve a sub-millimeter ground sampling distance (GSD) (<0.8 mm per pixel), the UAV was flown at a low altitude of approximately 6 m. The images obtained were then processed to create orthomosaic images in the GeoTIFF format, which involved a series of steps, including calibration and georeferencing [49].

The dataset comprising the UAV RGB images was processed through the Agisoft Metashape Professional software (version 1.8.2; Agisoft, St. Petersburg, Russia), aiming to produce a comprehensive orthomosaic image. The workflow within Metashape followed a structured sequence: aligning the photos for bundle adjustment, creating a dense point cloud, constructing a digital elevation model (DEM), and generating an orthomosaic image. Following the photo alignment phase, a detailed point cloud was assembled, drawing on the precise geographic (latitude and longitude) and orientational (altitude, pitch, and yaw) data recorded during the aerial survey. Utilizing this point cloud, a 3D polygonal mesh was crafted, and the DEM was developed from the mesh, with the spatial referencing set to the WGS84 ellipsoid and projected within the UTM zone 52. The RGB images resulted in a ground sampling distance of under 0.8 mm, as demonstrated in the processed data (Figure 3). The drone acquisition data is summarized in Table 1.

Table 1. Image acquisition of three species.

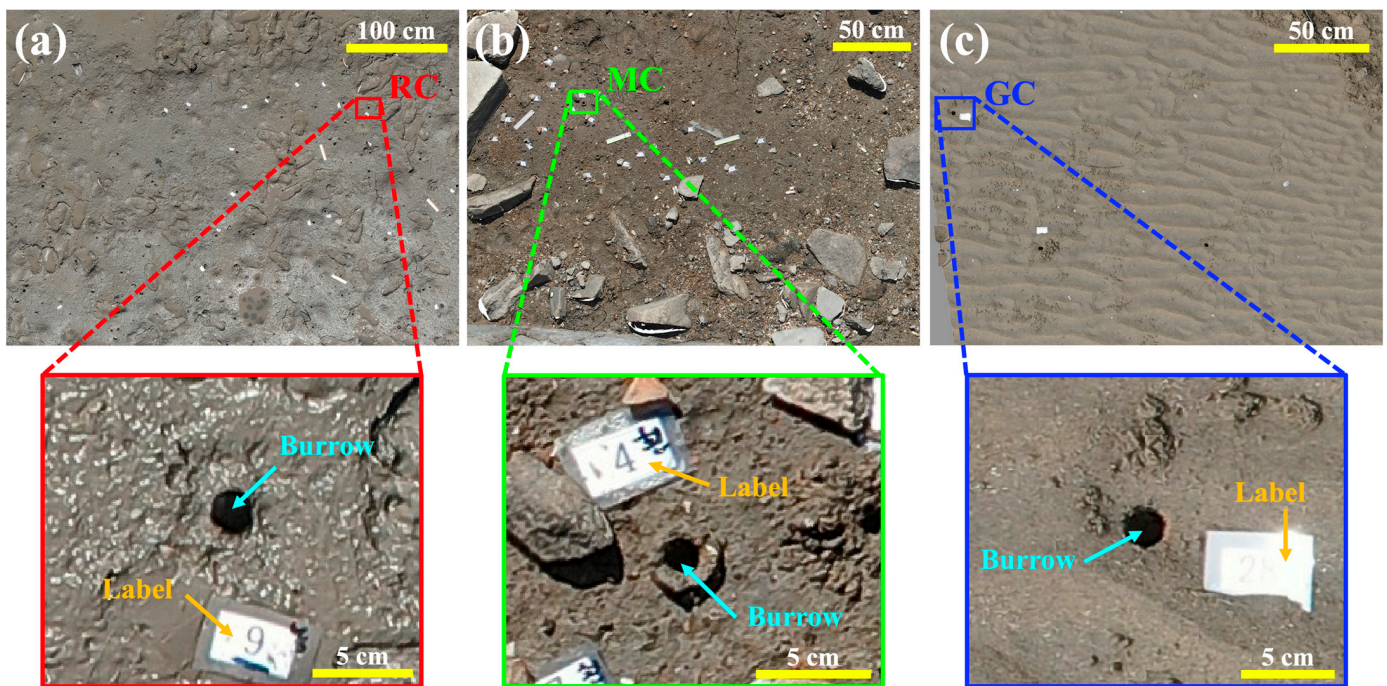|	Red-Clawed Fiddler Crab	Milky Fiddler Crab	Ghost Crab
Location (Sediment)	Mageumri (Mud)	Mageumri (Mud)	Sinduri (Sand)
Date and Time	16 August 2022 15:09:27	16 August 2022 11:24:08	14 August 2022 11:51:05
Area (m²)	4.0 × 5.3	4.3 × 6.5	12.7 × 15.5
Altitude (m)	6.0	6.0	6.0
Number of Photos	111	112	1302
Overlap (%)	65	65	65
Sidelap (%)	85	85	85
Sensor	Zenmuse P1 35 mm		
GSD (mm)	0.76	0.76	0.65

Figure 3. Examples of orthoimages and labeling with number markers: (**a**) red-clawed fiddler crab, (**b**) milky fiddler crab, and (**c**) ghost crab.

2.2.2. In Situ Field Data

Prior to the aerial image capture, direct in situ measurements of the burrow openings were taken to establish ground truth data for validation purposes. Burrows were selected for measurement based on clear indications of their active use, evidenced by fresh feeding debris and species-specific foraging trails. This selection criterion was critical to ensure that the measurements reflected current and active biological processes.

The species-specific burrow opening characteristics and associated feeding patterns facilitated accurate species identification. Precision in measuring the diameter of the burrow openings was achieved using digital calipers (Figure 4). To mitigate potential variability and ensure reliability, each burrow opening was measured three times. The mean value of these three measurements was then calculated and recorded as the definitive diameter for each burrow.
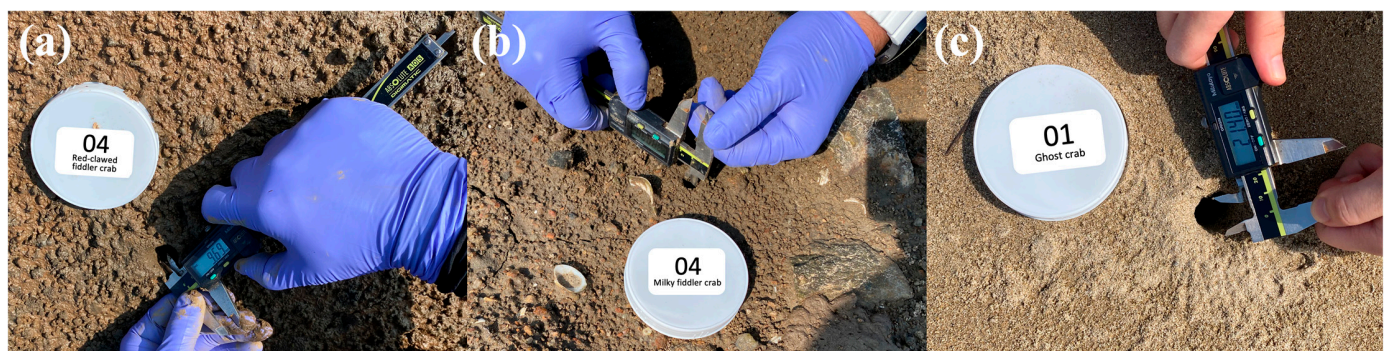

Figure 4. Examples of direct in situ measurements using digital calipers. (**a**) Red-clawed fiddler crab, (**b**) milky fiddler crab, and (**c**) ghost crab.

To correlate the in situ data with remote imagery, numbered markers were placed at each measured burrow to serve as reference points within the orthoimages (Figure 3). The drone flight for image acquisition was scheduled immediately after field measurements to capture the burrow openings in conditions that closely resembled those observed during

the field survey. This methodology was designed to capture the dynamic nature of the tidal flats and the organisms within. By closely synchronizing the in situ measurements with the drone imaging, we ensured a high degree of accuracy in representing the burrow openings, taking into account the biological activity of the macroinvertebrates that could influence the structural integrity and appearance of their burrows.

3. Methods

3.1. Image Annotation

The annotation process was meticulously carried out in a laboratory setting, where individual bounding boxes were delineated around each burrow opening identified within the orthoimages. Burrow openings that were either not visible due to the angle of capture or obscured by the organisms themselves were excluded to ensure the accuracy of the dataset. For each species identified, a detailed metadata record was created and stored in XML format. These metadata encompassed the dimensions of the bounding boxes in pixels, including the number of pixels along the x and y axes of the original image and the bounding boxes' maximum and minimum coordinates on these axes, as determined by the field measurements.

Field surveys provided measurements for a total of 20 samples each of the milky fiddler crabs (*Uca lactea*) and red-clawed fiddler crabs (*Uca arcuata*), and 30 samples of the ghost crabs (*Ocypode stimpsoni*). However, due to visibility issues in the drone-captured images, the final analysis included data from 12 red-clawed fiddler crabs, 17 milky fiddler crabs, and 25 ghost crabs. Table 2 summarizes the dataset utilized in this study, reflecting the meticulous selection process to ensure data quality and relevance.

Table 2. Datasets for each species.

Species	Study Area	Data	Sample
Red-clawed fiddler crab (*U. arcuata*)	Mageumri	U.arcuata.tif	12
		U.arcuata.xml	12
		U.arcuata.csv	20
Milky fiddler crab (*U. lactea*)	Mageumri	U.lactea.tif	17
		U.lactea.xml	17
		U.lactea.csv	20
Ghost crab (*O. stimpsoni*)	Sinduri	O.stimpsini_10.tif O.stimpsoni_28.tif O.stimpsoni_51.tif	25
		O.stimpsoni_10.xml O.stimpsoni_28.xml O.stimpsoni_51.xml	25
		O.stimpsoni.csv	30

3.2. Burrow Opening Extraction and Measurement

The process of extracting and measuring burrow openings was meticulously conducted using annotated orthoimages. Individual bounding boxes, corresponding to the burrow locations identified within the images, were extracted (Figure 5a,b). In these images, the burrow openings are distinguishable by their low reflectance, appearing darker compared to the brighter, higher reflectance of the surrounding sediment (Figure 5b). This difference in reflectance, quantified by digital number (DN) values, facilitated the feature differentiation within the imagery.
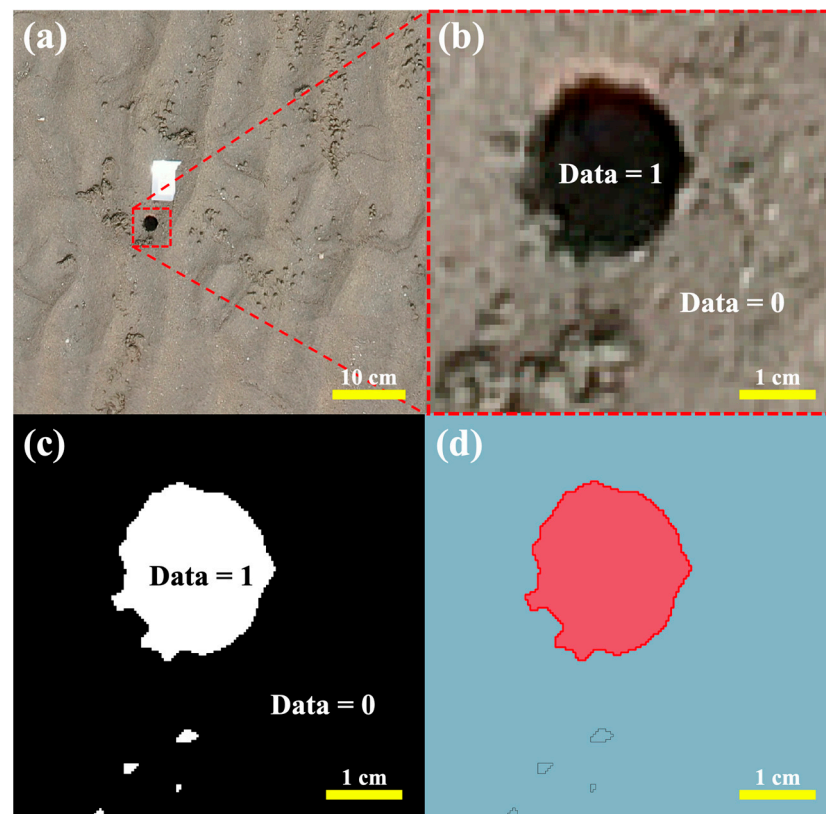
Figure 5. Image processing: (**a**) orthoimage of ghost crab sample 28, (**b**) cut image, (**c**) binary image, and (**d**) vector file.

The segmented images, aligning with the in situ measurement labels, were further processed to isolate the burrow openings, resulting in the binary images illustrated (Figure 5c). RGB-DN histograms (Figure 6) played a pivotal role in this process, enabling the distinction between the dark burrow openings and the brighter sedimentary background. This distinction was evident through two significant peaks in the histogram, corresponding to the contrast in reflectance. The histogram analysis involved identifying the lowest DN value of the first peak as the baseline and extracting a threshold at the 98th percentile of the normal distribution from this baseline. This threshold value was used to discern burrow openings from the sedimentary background, with pixels below this threshold selected for detailed analysis.

To enhance segmentation accuracy, threshold values were dynamically adjusted based on the unique characteristics of each species and individual burrows. The data extracted from this process were organized into text and image files, followed by a raster-to-vector conversion or polygonization, generating shapefiles for further analysis (Figure 5d).

During the extraction phase, our analysis faced the challenge of distinguishing genuine burrow openings from non-burrow features, such as shadows and sediments, which can exhibit similar reflectance values. To overcome this, we first extracted all objects based on their low reflectance peaks using the thresholds. Subsequently, to refine our results and enhance the accuracy of burrow detection, we implemented a sophisticated filtering step that relied on the geometric characteristics of the objects detected. By converting these images into shape files, we focused on the complexity of the objects' perimeters. Specifically, the number of vertices of each object became a critical factor in its classification. We hypothesized that objects with a higher number of vertices were more likely to be genuine burrow openings, as these were typically the largest features in the cut images (Figure 5c). Conversely, objects with simpler, smaller perimeters exhibiting fewer vertices were likely to be non-burrow features, such as shadows or sediment deposits, and were systematically classified as such and removed from further analysis. This method effectively minimized

the inclusion of irrelevant features and ensured that only potential burrow openings were retained for subsequent analysis.
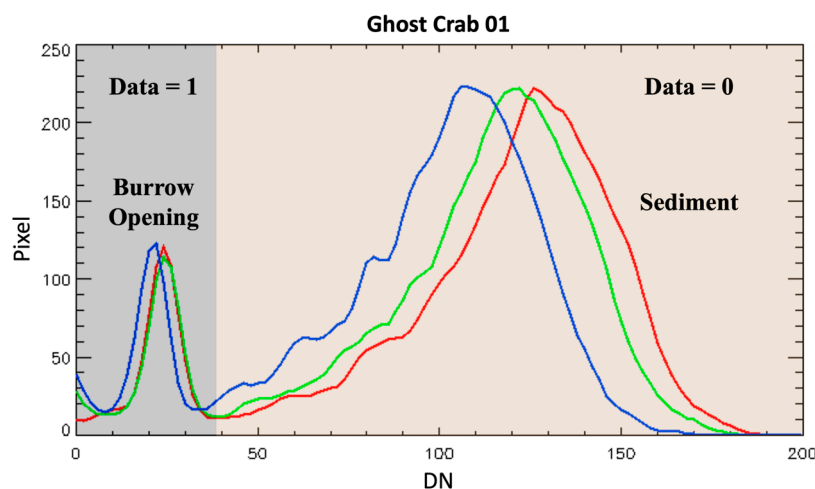

Figure 6. Example of RGB-DN histogram: ghost crab of sample 1. The red line, green line, and blue line represent the reflectance of the red band, green band, and blue band.

4. Results

4.1. Estimation of Burrow Opening Diameters

The final vector files facilitated the quantitative extraction of burrow opening diameters, employing a methodology that ensured high precision in distinguishing between true burrow openings and other similar appearing features. Considering the inherent circular geometry of the burrow openings characteristic of the species under study, our methodology focused on measuring the longest diameter of these openings. This approach was meticulously adopted to ensure the utmost precision in our quantitative analysis, allowing for an accurate representation of the burrow sizes. The methodology for estimating the diameters of circular burrow openings involved precisely identifying and marking the two furthest points along the perimeter of each opening.

The diameter of the circle was defined as the maximum distance between any two vertices of the shape (Figure 7). The central point of each burrow was determined by identifying the midpoint of the line segment connecting the two vertices that define this maximum distance. These terminal points, indicative of the maximum span of the diameter, were annotated with green rhombuses on the images (Figures 8–10). A solid blue line, connecting these points, visually represented the diameter of each burrow opening. Additionally, the midpoint of this diameter line, serving as the geometric center of the burrow opening, was highlighted with a red rhombus.

To accurately delineate the actual boundary of each burrow opening, circles were constructed so that their circumferences precisely passed through the terminal points of the diameter. These circles, outlined with solid red lines, effectively encapsulate the true extent of the burrow openings. The graphical depictions of these measurements, incorporating the annotated points and circles, were then saved in the PNG format for archival and further analysis.

This approach allowed for a standardized, geometrically accurate method of determining the diameters of the burrow openings, facilitating consistent comparisons across the dataset.
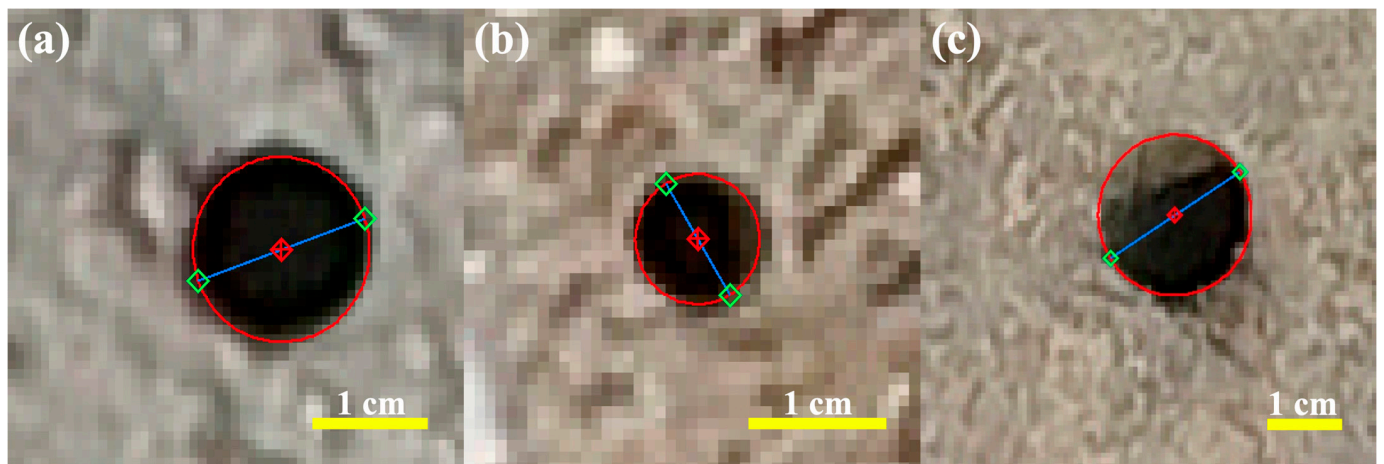
Figure 7. The results of extracted burrow openings. The red rhombuses, green rhombuses, blue lines, and red circles represent the center of the burrow opening, both ends of the diameter, the burrow opening diameter, and the edge of the burrow opening, respectively. (**a**) Red-clawed fiddler crab, (**b**) milky fiddler crab, and (**c**) ghost crab.
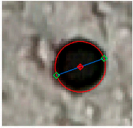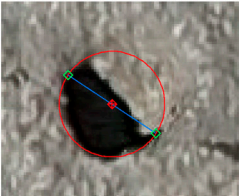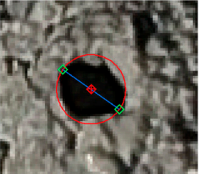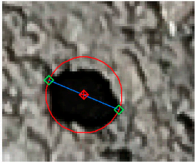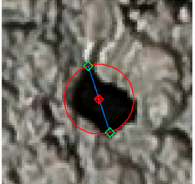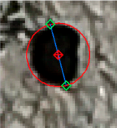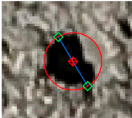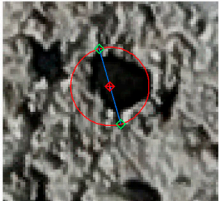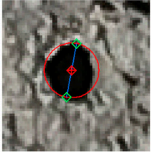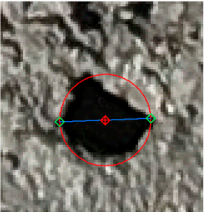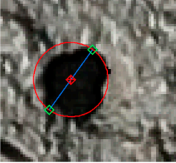

Figure 8. The results of 12 red-clawed fiddler crabs. The red rhombuses, green rhombuses, blue lines, and red circles represent the center of the burrow opening, both ends of the diameter, the burrow opening diameter, and the edge of the burrow opening, respectively.

MC-01	MC-02	MC-03	MC-04	MC-05
36 × 37 pixels	33 × 32 pixels	33 × 42 pixels	44 × 27 pixels	46 × 49 pixels
MC-06	MC-08	MC-10	MC-11	MC-12
30 × 39 pixels	33 × 37 pixels	31 × 35 pixels	33 × 40 pixels	33 × 28 pixels
MC-13	MC-14	MC-15	MC-17	MC-18
36 × 41 pixels	40 × 43 pixels	39 × 36 pixels	39 × 38 pixels	39 × 38 pixels
MC-19	MC-20			
43 × 43 pixels	46 × 48 pixels			

1 cm

Figure 9. The results of 17 milky fiddler crabs. The red rhombuses, green rhombuses, blue lines, and red circles represent the center of the burrow opening, both ends of the diameter, the burrow opening diameter, and the edge of the burrow opening, respectively.

GC-01	GC-02	GC-03	GC-04	GC-06
96 × 73 pixels	64 × 74 pixels	79 × 87 pixels	82 × 86 pixels	79 × 74 pixels
GC-07	**GC-08**	**GC-09**	**GC-11**	**GC-12**
82 × 104 pixels	69 × 78 pixels	90 × 68 pixels	59 × 68 pixels	72 × 91 pixels
GC-13	**GC-14**	**GC-15**	**GC-16**	**GC-17**
67 × 67 pixels	70 × 70 pixels	78 × 80 pixels	78 × 80 pixels	74 × 82 pixels
GC-18	**GC-19**	**GC-22**	**GC-23**	**GC-24**
92 × 103 pixels	63 × 57 pixels	78 × 80 pixels	89 × 99 pixels	79 × 95 pixels
GC-25	**GC-26**	**GC-28**	**GC-29**	**GC-30**
73 × 74 pixels	87 × 92 pixels	77 × 83 pixels	93 × 84 pixels	70 × 76 pixels

2 cm

Figure 10. The results of 25 ghost crabs. The red rhombuses, green rhombuses, blue lines, and red circles represent the center of the burrow opening, both ends of the diameter, the burrow opening diameter, and the edge of the burrow opening, respectively.
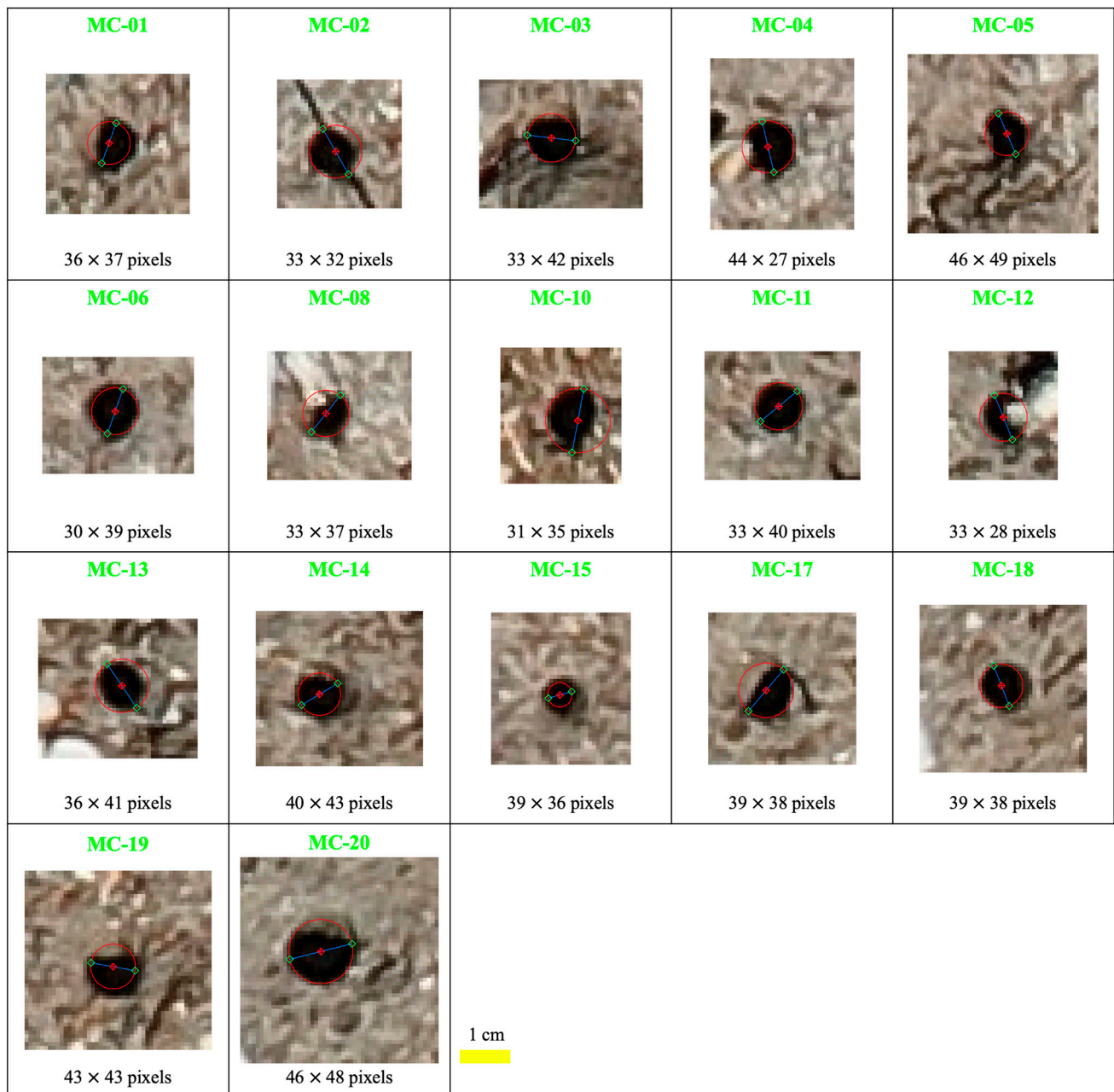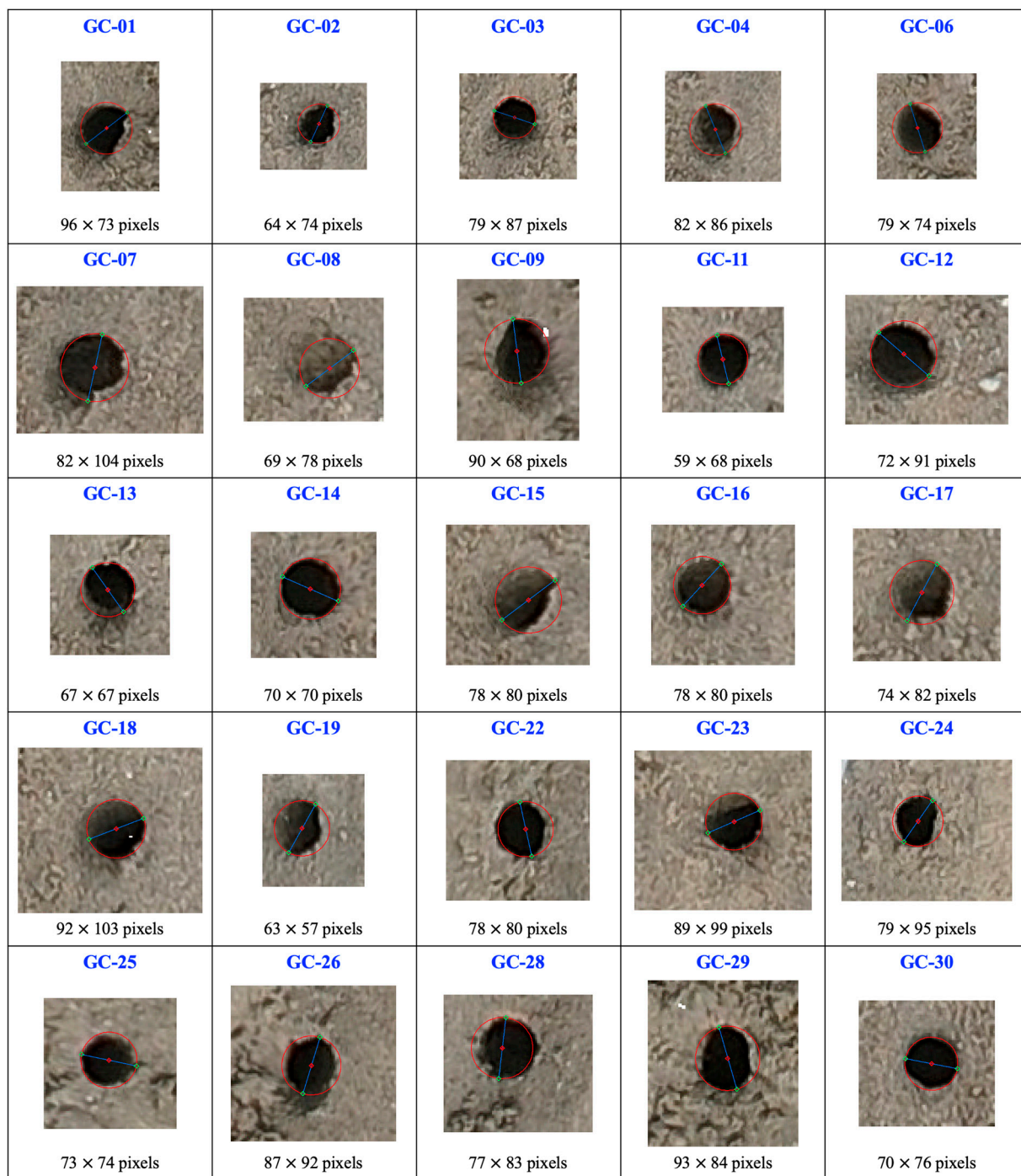
4.2. Validation

Validation of the estimated burrow opening diameters was conducted through a detailed comparison with in situ measurements at both the Mageumri and Sinduri tidal flats. At Mageumri, we analyzed the burrow openings of 12 red-clawed fiddler crabs and 17 milky fiddler crabs, revealing average diameters of 22.84 mm and 9.50 mm, respectively. Similarly, at Sinduri, 25 ghost crab burrow openings were labeled, with an average diameter of 22.36 mm observed.

To ensure the validity of our results, we compared these actual measurements against our model estimates (Figure 11). Each burrow opening's diameter was measured three times along its major axis, with the average of these measurements serving as the benchmark for validation. The root mean squared error (RMSE) values, indicative of the model's precision, were calculated for each species: 2.58 mm for the red-clawed fiddler crabs, 1.14 mm for the milky fiddler crabs, and 1.38 mm for the ghost crabs. An aggregate RMSE of 1.67 mm across all species underscores the model's overall accuracy.
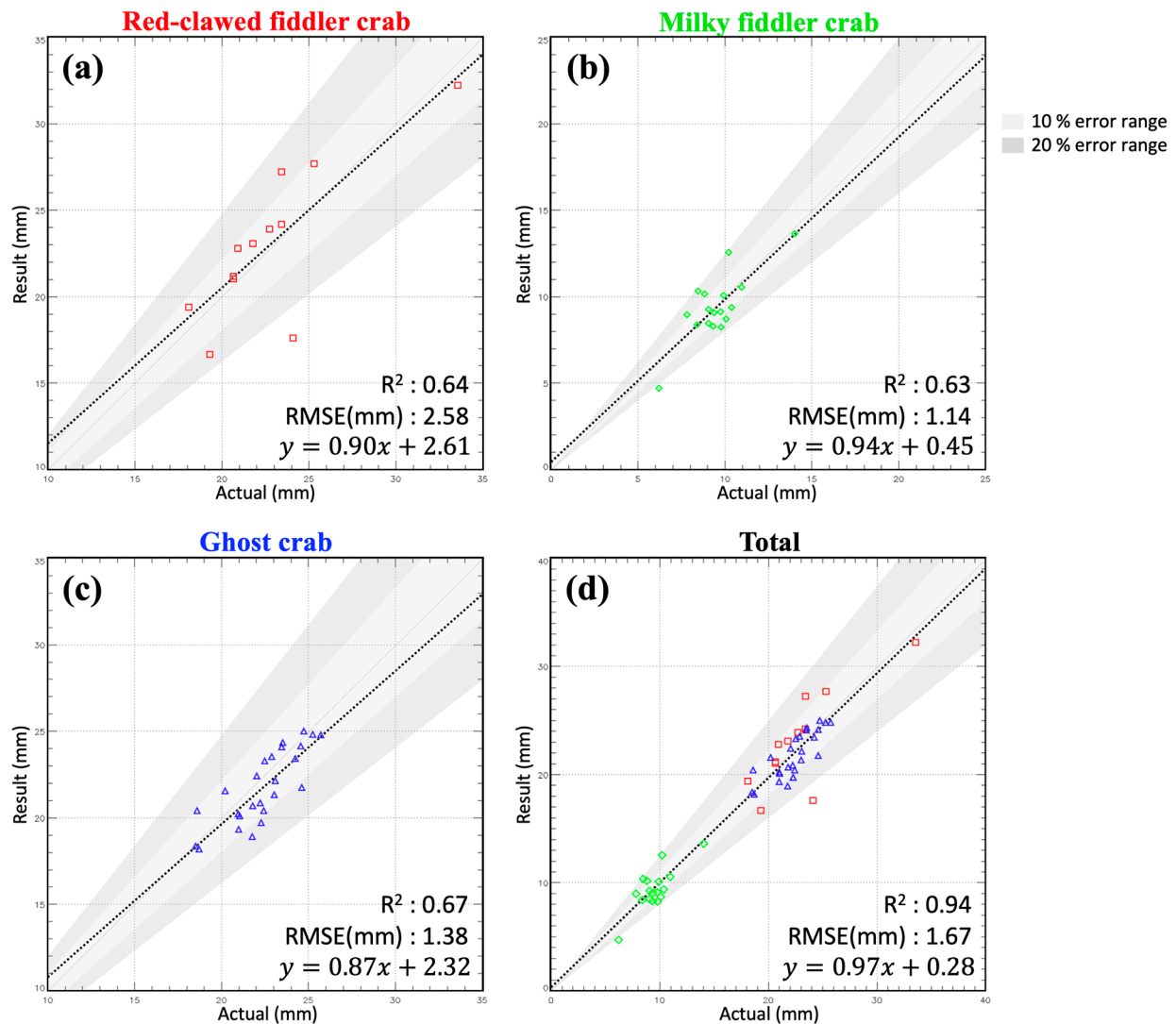

Figure 11. The relationship and RMSE between the actual measurement and the results. (**a**) Red-clawed fiddler crab, (**b**) milky fiddler crab, (**c**) ghost crab, and (**d**) total of the three species. Red, green, and blue represent the red-clawed fiddler, milky fiddler, and ghost crab, respectively. The grey areas indicate regions with an error range. The black dotted lines indicate the linear regression between the actual measurement and the results.

The correlation coefficient (R^2) between the actual measurements and the model estimates varied by species, reflecting the model's ability to predict burrow sizes accurately. The highest correlation was observed with the ghost crabs ($R^2 = 0.67$), followed by the red-clawed fiddler crabs ($R^2 = 0.64$) and milky fiddler crabs ($R^2 = 0.63$). Collectively, the R^2 value for all species was 0.94, demonstrating a strong overall correlation between the measured and estimated diameters, as detailed in Table 3. Most discrepancies between the model estimates and actual measurements fell within a 10–20% range, validating the effectiveness of our methodology in accurately estimating burrow opening diameters. We

demonstrated the capability to precisely measure burrow openings down to a minimum size of 6.21 mm, utilizing high-resolution drone imagery with an exceptional resolution of approximately 0.8 mm.

Table 3. Comparison of the R^2 and RMSE among the opening diameters of the three species.

Species	Range (mm)	Mean (mm)	R^2	RMSE (mm)
Red-clawed fiddler crab (*Uca arcuata*)	18.10–33.59	22.84	0.64	2.58
Milky fiddler crab (*Uca lactea*)	6.21–14.02	9.50	0.63	1.14
Ghost crab (*Ocypode stimpsoni*)	18.50–25.72	22.36	0.67	1.38
Total	6.21–33.59	18.42	0.94	1.67

5. Discussion

In this study, we quantified burrow opening sizes by exploiting the reflectance differences between the burrow openings and the surrounding sediment using drone remote sensing. This approach involved extracting burrow openings from RGB drone images and measuring their diameters based on their shape characteristics. The results demonstrate the capability to measure the diameters of burrow openings, ranging from 6.21 to 33.59 mm, with an RMSE of 1.67 mm and a correlation coefficient of 0.94, achieving error within 20%. In cases where the burrow openings were obscured by the inhabiting organisms (e.g., MC-12 in Figure 9) or deformed (e.g., RC-05 in Figure 8), resulting in a non-circular appearance in the drone imagery, our methodology allowed for the restoration of the true shape of these burrow openings. By employing advanced image processing techniques, we can discern and reconstruct the actual dimensions and shapes of the burrow openings, thereby overcoming potential biases introduced by visual obstructions or alterations. The use of UAVs represents a shift from traditional, labor-intensive field surveys to a more efficient, non-invasive approach that can cover extensive areas with minimal disturbance to the habitat. This methodology not only enhances the precision of biomass estimations and species distribution analyses but also enables for the conservation and management of tidal flat ecosystems.

Two samples, RC_13 and MC_15, yielded results outside of the 20% error margin. For RC_13, the discrepancy can be attributed to changes in the shape of the burrow opening caused by the residing organism between the time of measurement and the photography. Despite conducting the photography sessions immediately after the measurements to mitigate this issue, the burrow openings were altered due to human intrusion during the measurement process. On the other hand, MC_15, the smallest sample in our study with the actual measurement of 6.21 mm, was measured smaller at 4.71 mm when extracted using high-resolution UAVs imagery (GSD = 0.76 mm). This resulted in an error of 1.50 mm, equivalent to approximately a 2-pixel discrepancy in the image. These instances highlight the challenges in accurately capturing burrow opening dimensions, particularly when dealing with small sizes and the dynamic nature of intertidal zone habitats.

The milky fiddler crab, despite demonstrating the lowest RMSE (1.14 mm), exhibited a low correlation coefficient (R^2 = 0.63) (Figure 10). This result can be attributed to the fact that, compared to other species, the milky fiddler crab typically constructs the smallest burrow openings. Furthermore, the variation in the size of these burrows was limited, predominantly ranging between 7.81 mm and 10.96 mm, with a narrow span of 3.15 mm, excluding the smallest burrows. Enhancing the resolution of drone imagery could lead to improved outcomes in measuring smaller features. This improvement can be accomplished by either lowering the flight altitude to capture finer details or by employing advanced sensors with higher resolution capabilities, thereby significantly enhancing the quality and detail of the captured images.

Challenges in burrow extraction arose when remnant water was present within the burrows or when the internal shadows of the burrows were not distinctly visible due to the solar altitude. Notably, when remnant water was present inside the burrows, the interior appeared brighter, resulting in the absence of a dual-peak representation on the reflectance histogram. To obtain clear images of burrow openings, imaging should be scheduled after the lowest tide to ensure that the burrows are as free of water as possible. This approach enables the precise identification of features in the RGB images by leveraging clear differences in the reflectance. Furthermore, analyzing stacked multi-temporal images, captured at various times in the short term, can address the issue of inaccuracies in the representation of burrow openings in the drone images caused by shadows. By overlaying multi-temporal images, it becomes possible to mitigate these distortions. This method allows for a more accurate depiction of the burrow openings, as temporal variations in lighting and water conditions are averaged out or eliminated in the composite image.

The utilization of high-resolution drone-derived digital elevation model (DEM) data presents a strategic advantage to mitigate these challenges. High-resolution DEM data can facilitate the identification of burrow openings, which are generally recessed compared to the surrounding sediment. This method can leverage the elevation differences captured by the DEM to distinguish burrow openings from the adjacent sediment, providing a reliable means of detection unaffected by the visual impediments. Incorporating both optical RGB imagery and DEM data can enhance the robustness and accuracy of our approach, providing a comprehensive methodology for the detailed study of inter-tidal habitats.

The potential of drone imagery extends beyond morphological assessments, with emerging applications in species classification through machine learning. This approach, while adept at identifying species based on burrow morphology, currently lacks the capability to analyze quantitative features, such as size and diameter, comprehensively. Integrating machine learning with the methodologies outlined in this study could enable a more holistic analysis of tidal flat ecosystems, negating the need for invasive sampling techniques.

Future research should extend to burrows with non-circular openings, such as japanese ghost crab (*Macrophthalmus japonicus*) and granulate-hand ghost crab (*Macrophthalmus dilatatus*), exploring how different shapes relate to species' size, foraging behavior, and biomass implications. Such investigations could enhance our understanding of ecosystem dynamics and contribute to the precision of remote sensing techniques in ecological studies, where the accurate characterization of minute environmental features is crucial.

6. Conclusions

This study showcases the effective application of drone-based high-resolution optical imagery for measuring the burrow openings of intertidal macroinvertebrates, marking a significant advancement in remote sensing methodologies applied to ecological research. We have demonstrated the capability to measure burrow openings ranging from a few millimeters to a few centimeters in size, with an error margin within 20%. The drone system, with its millimeter resolution, enables detailed classification of macroinvertebrate species and measurements of an organism's size. Our method showcases its robustness and accuracy in quantifying the diameter of burrow openings, a critical factor in understanding the ecology of intertidal zones. Such advancements are anticipated to see increased utilization, particularly in macroinvertebrate ecology, where they can significantly contribute to the assessment of organisms' size, weight, growth rate, and biomass.

Future research should focus on broadening the applicability of our UAV-derived remote sensing methodology to a wider range of species and environmental contexts. It is essential to refine the precision of our measurements and to explore the integration of further remote sensing technologies alongside machine learning algorithms. Recent studies have successfully utilized artificial intelligence and high-resolution UAV imagery, enabling the precise identification and classification of burrow openings and their associated species [50,51]. By incorporating these advanced AI techniques into our methodology, we expect to significantly broaden the scope and depth of research of tidal flat ecosys-

tems. Additionally, we look forward to the development of quieter or even silent drone technologies and improved sensors with enhanced field of view (FOV) characteristics. Advancements in these areas could enable higher-altitude flights, thus reducing the potential for disturbance and enhancing the feasibility of using drones for ecological research. Consequently, our study not only introduces a novel tool for ecological monitoring but also highlights the potential of sophisticated remote sensing techniques integrated with ecological research to tackle complex environmental challenges. This promising integration is set to transform our understanding of ecological dynamics and contribute substantially to the conservation and management of vulnerable coastal habitats.

Data Availability Statement: The original contributions presented in the study are included in the article, further inquiries can be directed to the corresponding author.

Conflicts of Interest: The authors declare no conflict of interest.

References

1. McLeod, E.; Chmura, G.L.; Bouillon, S.; Salm, R.; Björk, M.; Duarte, C.M.; Lovelock, C.E.; Schlesinger, W.H.; Silliman, B.R. A blueprint for blue carbon: Toward an Improved Understanding of the Role of Vegetated Coastal Habitats in Sequestering CO_2. *Front. Ecol. Environ.* **2011**, *9*, 552–560. [CrossRef] [PubMed]
2. Macreadie, P.I.; Anton, A.; Raven, J.A.; Beaumont, N.; Connolly, R.M.; Friess, D.A.; Kelleway, J.J.; Kennedy, H.; Kuwae, T.; Lavery, P.S.; et al. The future of Blue Carbon science. *Nat. Commun.* **2019**, *10*, 3998. [CrossRef] [PubMed]
3. Brown, D.R.; Marotta, H.; Peixoto, R.B.; Enrich-Prast, A.; Barroso, G.C.; Soares, M.L.G.; Machado, W.; Pérez, A.; Smoak, J.M.; Sanders, L.M. Hypersaline Tidal Flats as Important "Blue Carbon" Systems: A Case Study from Three Ecosystems. *Biogeosciences* **2021**, *18*, 2527–2538. [CrossRef]
4. Heip, C.H.R.; Goosen, N.K.; Herman, P.M.J.; Kromkamp, J.; Middelburg, J.J.; Soetaert, K. Production and Consumption of Biological Particles in Temperate Tidal Estuaries. In *Oceanography and Marine Biology: An Annual Review*; UCL Press: London, UK, 1995.
5. N-Uptake, A. Primary Production by Phytoplankton and Microphytobenthos in Estuaries. *Estuaries* **1999**, *29*, 93.
6. Forja, J.M.; Ortega, T.; DelValls, T.A.; Gómez-Parra, A. Benthic Fluxes of Inorganic Carbon in Shallow Coastal Ecosystems of the Iberian Peninsula. *Mar. Chem.* **2004**, *85*, 141–156. [CrossRef]
7. Chmura, G.L.; Anisfeld, S.C.; Cahoon, D.R.; Lynch, J.C. Global Carbon Sequestration in Tidal, Saline Wetland Soils. *Glob. Biogeochem. Cycles* **2003**, *17*, 1111. [CrossRef]
8. Kuipers, B.R.; De Wilde, P.A.W.J.; Creutzberg, F. Energy Flow in a Tidal Flat Ecosystem. *Mar. Ecol. Prog. Ser.* **1981**, *5*, 215–221. [CrossRef]
9. Lin, W.-J.; Wu, J.; Lin, H.-J. Contribution of Unvegetated Tidal Flats to Coastal Carbon Flux. *Glob. Chang. Biol.* **2020**, *26*, 3443–3454. [CrossRef] [PubMed]
10. Guarini, J.-M.; Chauvaud, L.; Coston-Guarini, J. Can the Intertidal Benthic Microalgal Primary Production Account for the "Missing Carbon Sink"? *J. Oceanogr. Res. Data* **2008**, *1*, 13–19.
11. Jordan, T.E.; Valiela, I. A Nitrogen Budget of the Ribbed Mussel, Geukensia Demissa, and Its Significance in Nitrogen Flow in a New England Salt Marsh 1. *Limnol. Oceanogr.* **1982**, *27*, 75–90. [CrossRef]
12. Jones, C.G.; Lawton, J.H.; Shachak, M. Organisms as Ecosystem Engineers. *Oikos* **1994**, *69*, 373–386. [CrossRef]
13. Levinton, J. Bioturbators as ecosystem engineers: Control of the Sediment Fabric, Inter-individual Interactions, and Material Fluxes. In *Linking Species & Ecosystems*; Springer: Boston, MA, USA, 1995; pp. 29–36.
14. Kostka, J.E.; Gribsholt, B.; Petrie, E.; Dalton, D.; Skelton, H.; Kristensen, K. The Rates and Pathways of Carbon Oxidation in Bioturbated Saltmarsh Sediments. *Limnol. Oceanogr.* **2002**, *47*, 230–240. [CrossRef]
15. Kogure, K.; Wada, M. Impacts of Macrobenthic Bioturbation in Marine Sediment on Bacterial Metabolic Activity. *Microbes Environ.* **2005**, *20*, 191–199. [CrossRef]

16. Andreetta, A.; Fusi, M.; Cameldi, I.; Cimò, F.; Carnicelli, S.; Cannicci, S. Mangrove Carbon Sink. Do Burrowing Crabs Contribute to Sediment Carbon Storage? Evidence from a Kenyan Mangrove System. *J. Sea Res.* **2014**, *85*, 524–533. [CrossRef]

17. Qiu, D.; Cui, B.; Yan, J.; Ma, X.; Ning, Z.; Wang, F.; Sui, H.; Bai, J. Effect of Burrowing Crabs on Retention and Accumulation of Soil Carbon and Nitrogen in an Intertidal Salt Marsh. *J. Sea Res.* **2019**, *154*, 101808. [CrossRef]

18. Sasaki, A.; Nakao, H.; Yoshitake, S.; Nakatsubo, T. Effects of the burrowing mud shrimp, *Upogebia yokoyai*, on carbon flow and microbial activity on a tidal flat. *Ecol. Res.* **2014**, *29*, 493–499. [CrossRef]

19. Agusto, L.E.; Qin, G.; Thibodeau, B.; Tang, J.; Zhang, J.; Zhou, J.; Wu, J.; Zhang, L.; Thapa, P.; Wang, F.; et al. Fiddling with the Blue Carbon: Fiddler Crab Burrows Enhance CO_2 and CH_4 Efflux in Saltmarsh. *Ecol. Indic.* **2022**, *144*, 109538. [CrossRef]

20. Schlacher, T.A.; Lucrezi, S.; Peterson, C.H.; Connolly, R.M.; Olds, A.D.; Althaus, F.; Hyndes, G.A.; Maslo, B.; Gilby, B.L.; Leon, J.X. Estimating Animal Populations and Body Sizes from Burrows: Marine Ecologists Have Their Heads Buried in the Sand. *J. Sea Res.* **2016**, *112*, 55–64. [CrossRef]

21. Butler, S.; Bird, F.L. Estimating Density of Intertidal Ghost Shrimps Using Counts of Burrow Openings. Is the Method Reliable? *Hydrobiologia* **2007**, *589*, 303–314. [CrossRef]

22. Beukema, J.J. Biomass and Species Richness of the Macro-Benthic Animals Living on the Tidal Flats of the Dutch Wadden Sea. *Neth. J. Sea Res.* **1976**, *10*, 236–261. [CrossRef]

23. Nickell, L.A.; Atkinson, R.J.A. Functional Morphology of Burrows and Trophic Modes of Three Thalassinidean Shrimp Species, and a New Approach to the Classification of Thalassinidean Burrow Morphology. *Mar. Ecol. Prog. Ser.* **1995**, *128*, 181–197. [CrossRef]

24. Koo, B.J.; Seo, J.; Jang, M.S. The Relationship between Burrow Opening Dimensions and Biomass of Intertidal Macroinvertebrates by Feeding Mode (Surface Deposit Feeders vs. Suspension Feeders). *Animals* **2022**, *12*, 2878. [CrossRef]

25. Guo, M.; Li, J.; Sheng, C.; Xu, J.; Wu, L. A Review of Wetland Remote Sensing. *Sensors* **2017**, *17*, 777. [CrossRef] [PubMed]

26. Ozesmi, S.L.; Bauer, M.E. Satellite Remote Sensing of Wetlands. *Wetl. Ecol. Manag.* **2002**, *10*, 381–402. [CrossRef]

27. Lahoz-Monfort, J.J.; Guillera-Arroita, G.; Milner-Gulland, E.J.; Young, R.P.; Nicholson, E. Satellite Imagery as a Single Source of Predictor Variables for Habitat Suitability Modelling: How Landsat Can Inform the Conservation of a Critically Endangered Lemur. *J. Appl. Ecol.* **2010**, *47*, 1094–1102. [CrossRef]

28. Tseng, K.-H.; Kuo, C.-Y.; Lin, T.-H.; Huang, Z.-C.; Lin, Y.-C.; Liao, W.-H.; Chen, C.-F. Reconstruction of Time-Varying Tidal Flat Topography Using Optical Remote Sensing Imageries. *ISPRS J. Photogramm. Remote Sens.* **2017**, *131*, 92–103. [CrossRef]

29. Murray, N.J.; Phinn, S.R.; DeWitt, M.; Ferrari, R.; Johnston, R.; Lyons, M.B.; Clinton, N.; Thau, D.; Fuller, R.A. The Global Distribution and Trajectory of Tidal Flats. *Nature* **2019**, *565*, 222–225. [CrossRef] [PubMed]

30. Alvarez-Vanhard, E.; Corpetti, T.; Houet, T. UAV & Satellite Synergies for Optical Remote Sensing Applications: A Literature Review. *Sci. Remote Sens.* **2021**, *3*, 100019.

31. Brunetta, R.; Duo, E.; Ciavola, P. Evaluating Short-Term Tidal Flat Evolution through UAV Surveys: A Case Study in the Po Delta (Italy). *Remote Sens.* **2021**, *13*, 2322. [CrossRef]

32. Fairley, I.; Mendzil, A.; Togneri, M.; Reeve, D.E. The Use of Unmanned Aerial Systems to Map Intertidal Sediment. *Remote Sens.* **2018**, *10*, 1918. [CrossRef]

33. Anderson, K.; Gaston, K.J. Lightweight Unmanned Aerial Vehicles Will Revolutionize Spatial Ecology. *Front. Ecol. Environ.* **2013**, *11*, 138–146. [CrossRef] [PubMed]

34. Brunier, G.; Michaud, E.; Fleury, J.; Anthony, E.J.; Morvan, S.; Gardel, A. Assessing the Relationship etween Macro-faunal Burrowing Activity and Mudflat Geomorphology from UAV-based Structure-from-Motion Photogrammetry. *Remote Sens. Environ.* **2020**, *241*, 111717. [CrossRef]

35. Chen, C.; Tian, B.; Wu, W.; Duan, Y.; Zhou, Y.; Zhang, C. UAV Photogrammetry in Intertidal Mudflats: Accuracy, Efficiency, and Potential for Integration with Satellite Imagery. *Remote Sens.* **2023**, *15*, 1814. [CrossRef]

36. Ventura, D.; Bonifazi, A.; Gravina, M.F.; Belluscio, A.; Ardizzone, G. Mapping and Classification of Ecologically Sensitive Marine Habitats Using Unmanned Aerial Vehicle (UAV) Imagery and Object-Based Image Analysis (OBIA). *Remote Sens.* **2018**, *10*, 1331. [CrossRef]

37. Kim, K.; Lee, D.; Jang, Y.; Lee, J.; Kim, C.-H.; Jou, H.-T.; Ryu, J.-H. Deep Learning of High-Resolution Unmanned Aerial Vehicle Imagery for Classifying Halophyte Species: A Comparative Study for Small Patches and Mixed Vegetation. *Remote Sens.* **2023**, *15*, 2723. [CrossRef]

38. Henriques, M.; Catry, T.; Belo, J.R.; Piersma, T.; Pontes, S.; Granadeiro, J.P. Combining Multispectral and Radar Imagery with Machine Learning Techniques to Map Intertidal Habitats for Migratory Shorebirds. *Remote Sens.* **2022**, *14*, 3260. [CrossRef]

39. Kim, K.-L.; Woo, H.-J.; Jou, H.-T.; Jung, H.C.; Lee, S.-K.; Ryu, J.-H. Surface Sediment Classification Using a Deep Learning Model and Unmanned Aerial Vehicle Data of Tidal Flats. *Mar. Pollut. Bull.* **2024**, *198*, 115823. [CrossRef] [PubMed]

40. Lee, D.; Moon, H.; Seo, J.; Kim, K.; Kim, C.; Koo, B.J.; Ryu, J.-H.; Jou, H.-T. Research on Improving Object Detection Models for Macroinvertebrates Based on Machine Learning Using Tidal Flat UAV-Imagery. In Proceedings of the Geo AI Data Society 2023 Spring Conference, Busan, Republic of Korea, 27–29 June 2023.

41. Kim, D.-W.; Lee, S.-H.; Yu, J.-J.; Son, S.-W. Image analysis technology with deep learning for monitoring the tidal flat ecosystem—Focused on monitoring the Ocypode stimpsoni Ortmann, 1897 in the Sinduri tidal flat. *J. Korean Soc. Environ. Restor. Technol.* **2021**, *24*, 89–96.

42. Egawa, R.; Sharma, S.; Nadaoka, K.; MacKenzie, R.A. Burrow Dynamics of Crabs in Subtropical Estuarine Mangrove Forest. *Estuar. Coast. Shelf Sci.* **2021**, *252*, 107244. [CrossRef]

43. Zeil, J.; Hemmi, J.M. The Visual Ecology of Fiddler Crabs. *J. Comp. Physiol. A* **2006**, *192*, 1–25. [CrossRef]

44. Choi, J.-K.; Ryu, J.-H.; Eom, J.; Roh, S.-M.; Noh, J.H. Analysis on the Sedimentary Environment and Microphytobenthos Distribution in the Geunso Bay Tidal Flat Using Remotely Sensed Data. *J. Wetl. Res.* **2010**, *12*, 67–78.

45. Dembowski, J.B. Notes on the Behavior of the Fiddler Crab. *Biol. Bull.* **1926**, *50*, 179–201. [CrossRef]

46. Yun, K.; Lee, C.K.; Kim, G.S. Estimates on the Long-term Landform Changes Near Sinduri Beaches. *Korean J. Remote Sens.* **2022**, *38*, 1315–1328.

47. Koo, B.K.; Shin, S.H.; Woo, H.J. Distribution of Benthic Macrofauna in Subtidal Area and on Sand Flat of Sindu-ri Coast, Korea. *J. Wetl. Res.* **2005**, *7*, 69–88.

48. Chakrabarti, A. Burrow Patterns of Ocypode Ceratophthalma (Pallas) and Their Environmental Significance. *J. Paleontol.* **1981**, *55*, 431–441.

49. Nex, F.; Remondino, F. UAV for 3D Mapping Applications: A Review. *Appl. Geomat.* **2014**, *6*, 1–15. [CrossRef]

50. Bycroft, R.; Leon, J.X.; Schoeman, D. Comparing Random Forests and Convoluted Neural Networks for Mapping Ghost Crab Burrows Using Imagery from an Unmanned Aerial Vehicle. *Estuar. Coast. Shelf Sci.* **2019**, *224*, 84–93. [CrossRef]

51. Schenone, S.; Azhar, M.; Ramírez, C.A.V.; Strozzi, A.G.; Delmas, P.; Thrush, S.F. Mapping the Delivery of Ecological Functions Combining Field Collected Data and Unmanned Aerial Vehicles (UAVs). *Ecosystems* **2021**, *25*, 948–959. [CrossRef]